Exploiting the Photonic Crystal Properties of TiO$_2$ Nanotube Arrays to Enhance Photocatalytic Hydrogen Production

Gian Luca Chiarello,[†] *Alessio Zuliani,*[†] *Davide Ceresoli,*[§] *Rocco Martinazzo,*[†] *Elena Selli*[†]

[†] Università degli Studi di Milano, Dipartimento di Chimica, via Golgi 19, I-20133 Milano, Italy

[§] CNR-ISTM, Institute of Molecular Sciences and Technologies, via Golgi 19, I-20133 Milano, Italy

ABSTRACT Two series of self-assembled TiO$_2$ nanotube (NT) arrays were grown by electrochemical anodization on a metallic titanium substrate with different anodization times and applied potentials in HF-containing ethylene glycol electrolyte solutions, and post-calcined at 450 °C. The so obtained thin films were characterized by FESEM, XRD, UV-vis-NIR DRS analyses and tested as photoanodes in Incident Photon to Current Efficiency (IPCE) measurements and in a two compartment photoelectrochemical cell (PEC) for separate H$_2$ and O$_2$ production. The photocatalytic performance of the NT arrays significantly increased with increasing the potential applied during anodization (*i.e.*, with increasing the NT inner diameter). IPCE measurements reveal that such unexpected behavior is due to a red shift of the activity threshold that allows harvesting and converting a larger portion of the solar spectrum. This phenomenon is ascribed to the parallel shift of the photonic bandgap position originated by the

intrinsic photonic crystal properties and demonstrates the important role played by ordered hierarchical structures in improving the photocatalytic performance of NT arrays by confining and manipulating light.

1. INTRODUCTION

Photoelectrochemical cells (PECs) are the most promising devices for solar energy harvesting and storage in the form of hydrogen as solar fuel, because they allow water cleavage with separate H_2 and O_2 production.[1–6] Fabrication of stable and efficient photoelectrodes is the crucial task for the future development and application of such devices. Thin films consisting of self-assembled, vertically oriented TiO_2 nanotube (NT) arrays, directly grown on a conductive Ti foil by electrochemical anodization,[7,8] represent an attractive and cost-effective method to prepare photoanodes.[6,9–12] Their well-organized architecture provides: *i*) efficient percolation pathways for vectorial transfer of photopromoted electrons, ensuring effective charge separation; *ii*) large internal surface area which guarantees enhanced photon absorption and reactant adsorption on the photoactive surface; and *iii*) optimal adhesion of the photoactive film to the conductive support ensuring high stability and improved electron transfer.

The ordered 2D structure of the NT arrays confers them the photonic crystal properties due to the periodic modulation of the dielectric constant.[13–15] This provokes the formation of a photonic band gap (PBG), *i.e.* a range of forbidden wavelengths in certain directions that are totally reflected and cannot propagate through the periodic structure, due to Bragg diffraction and scattering. Moreover, the electromagnetic field is predominantly localized in the low-dielectric material (air or water) at the blue-edge of the PBG (air band), whereas it is predominantly localized on the high-dielectric material (TiO_2 NT walls) at the red-edge (dielectric band). A third important property of photonic crystal arises from the flattening of the air and dielectric bands in some directions. Because the group velocity of the photons is proportional to the slope of the dispersion curves at the high and low energy edges, light travels at a speed approaching zero where the photonic bands are flat, generating the so called "slow photons".[14,15]

Hence, the PBG can in principle be exploited in photocatalysis to confine, control, and manipulate photons with the intent to intensify the efficiency of light harvesting and absorption. The major effort in this field has been addressed towards 3D TiO_2 inverse opal structures.[16–21] However, only in few reports[22,23] the photonic crystal properties of TiO_2 NT films has been explored for photocatalytic applications despite the large number of publications on this topic.

The physicochemical properties and morphology of NTs can be easily tailored by controlling the synthesis parameters such as the anodization time, the applied DC voltage, the electrolyte composition and the thermal post-treatment conditions.[7] In this work we show, with the support of theoretical calculations, that the PBG position and width are affected by the NT inner diameter and wall thickness, and by the distance between the tubes. The PBG can be easily tuned in order to maximize the harvesting efficiency especially at the absorption edge. In particular, a linear red shift of the photoactivity edge with a consequently up to 50% increased photocatalytic H_2 production rate under polychromatic irradiation can be attained by simply increasing the NTs inner diameter (*i.e.*, red shifting the PBG) without any chemical doping or electronic structure modification.

2. METHODS

2.1 TiO$_2$ NT films preparation. Thin films of vertically oriented TiO_2 nanotube (NT) arrays self-assembled on a conductive Ti support were prepared by electrochemical anodization. A homemade electrochemical cell was employed consisting of a PVC conical bath with a 40 mm diameter hole at the bottom, placed on a stainless steel support. The hole is closed underneath with a 45×45 mm^2 Ti foil (Advent, temper annealed, purity 99.6 %, thickness 100 μm), firmly sealed against an O-ring by a screw with a plexiglass plaque on top. A copper wire is inserted between the Ti foil and the plexiglas to ensure electrical contact. A 45×45 mm^2 Pt mesh

(Goodfellow, 0.25 mm aperture, 65% open area) was used as counter electrode to allow the release of hydrogen gas produced underneath during the anodization process. The Pt mesh was immersed in the electrolyte solution and suspended 20 mm above the Ti foil. The Ti foil (anode) and the Pt counter electrode (cathode) were connected to a EA-PS 2384-05B power supply and a Tektronix DMM4040digital multimeter. Prior to anodization, the Ti foils were degreased and cleaned with acetone, then methanol, and finally with MilliQ water in an ultrasonic bath, for 15 min each.

A two-anodization process was employed in order to obtain more homogeneous TiO_2 NT films. During the first step, the samples were anodized at 35 V for 120 min in a 1.0 M H_2O + 0.1 M NH_4F in ethylene glycol electrolyte solution. The obtained TiO_2 NT film was removed by ultrasonic treatment in water. This step flattens the Ti foil surface and leaves a pattern of little grooves that helps the formation of more homogeneous NT films during the second anodization. A 8.0 M H_2O + 0.2 M HF in ethylene glycol electrolyte solution was used during the second anodization. In order to study the effect of the anodization time and applied voltage, two series of samples were prepared. In the first series the anodization time was changed from 10 min to 240 min, with a fixed applied voltage of 50 V. Because the NTs growing rate increases with increasing the applied voltage, in the second series the voltage was changed from 30 V up to 80 V while decreasing the anodization time, in order to obtain ca. 1 μm-long TiO_2 NTs. After the second anodization, the samples were washed in ethanol in the ultrasonic bath for 15 min and calcined in oven at 450 °C for 2 h, with a heating ramp of 10 °C min^{-1}.

2.2 Characterization of TiO_2 NT films. Scanning electron microscopy (SEM) analysis was carried out on a LEICA LEO 1430 instrument. Field emission scanning electron microscopy (FESEM) images were obtained with a ZEISS Supra40 apparatus. X-ray diffraction patterns

were recorded on a Philips PW3020 powder diffractometer, by using the Cu Kα radiation (λ= 1.5418 Å). UV-Vis-NIR diffuse reflectance (DR) spectra were recorded in the 220 nm $< \lambda <$ 2600 nm range with a Shimadzu UV3600 Plus spectrophotometer equipped with an ISR-603 integrating sphere.

2.3 IPCE measurements. Incident photon to current efficiency (IPCE) was measured on an optical bench equipped with a 300 W Xe lamp (Lot-Oriel), a monochromator (LOT-Oriel Omni-λ 150), a shutter (Thorlabs SC10) and a homemade plexiglas cell with a pyrex glass window. A 25×25 mm^2 platinum foil (cathode) was used as counter electrode and placed below the irradiated TiO_2 NT film (anode). Both cathode and anode were immersed in a 1.0 M NaOH electrolyte solution. The photocurrent was measured with a Tektronix DMM4040 digital multimeter in the 250-550 nm wavelength range with a 2 nm step and a 4 s time per step. The incident light power was measured with the same scan parameters using a calibrated Thorlabs S130VC photodiode connected to a Thorlabs PM200 power meter placed at exactly the same distance as the TiO_2 NT film, with the pyrex window in between to account for the transmittance of the cell window. The percent IPCE at each wavelength was calculated employing the following formula:

$$\% \, IPCE = \frac{I_\lambda}{P_\lambda} \cdot \frac{1240}{\lambda} \cdot 100$$

where I_λ is the short circuit photocurrent density (mA cm^{-2}) measured with the digital multimeter at a specific incident wavelength λ (nm), P_λ is the incident power density (mW cm^{-2}) measured with the photodiode at the same λ, and 1240 (J nm C^{-1}) $= h \, c \, e^{-1}$, h being the Planck constant, c the speed of light and e the charge of a single electron.

2.4 Separate H$_2$ and O$_2$ photocatalytic production tests. The synthetized TiO_2 NT films were tested as photoanodes in a two compartment photocatalytic cell for separate H$_2$ and O$_2$

production similar to that already described.[5] The cell allows one to simultaneously measure the evolved gases and the direct photocurrent. In particular, the TiO_2 NT photoanode was immersed in a 0.5 M H_2SO_4 solution (anodic compartment) and connected to a Pt counter electrode immersed in a 1.0 M NaOH solution, by an external circuit including a digital Tektronix DMM4040 multimeter. The two compartments were separated by an ion exchange Nafion 117 membrane. The irradiation source was an iron halogenide mercury arc lamp (Jelosil HG200, 250 W) emitting in the 350 nm $< \lambda <$ 450 nm range, with a full irradiation intensity of ca. 32 mW cm^{-2}. The emission spectrum of the lamp was measured by means of a Thorlabs CCS100 spectrometer with a compact CCD. The evolved H_2 and O_2 were collected in two graduated burettes surmounting the two electrodes, initially filled with the two electrolyte solutions; their volume was measured every 30 min irradiation from the displacement of the liquid inside the burettes. No electrical bias or sacrificial agent was ever employed during the tests.

2.5 Computational methods. The photonic band structure and the electromagnetic modes were calculated employing the MIT Photonic-Bands code (MPB).[24] The TiO_2 NTs periodic structure was modeled as a continuum with a frequency-independent isotropic dielectric constant of 7.13, equal to that of bulk anatase at 3 eV (*i.e.*, just below the absorption edge) as reported by Jellison, *et al.*[25] The adopted simulation was purely two-dimensional (*i.e.*, assuming NTs of infinite length) with a periodic array of spatially separated hollow cylinders with a hexagonal lattice arrangement. The effect of the three different geometrical parameters (inner radius from 10 to 100 nm, wall thickness from 6 to 20 nm, and gap between tubes from 10 to 40 nm) on the photonic bandgap position was investigated. When varying one parameter the other two were set as follows: the inner radius at 50 nm, the tube thickness at 10 nm, and the distance between tube

walls at 20 nm. The empty space was assumed to have a dielectric constant of 1.7, to model the effect of interstitial water.

3. RESULTS AND DISCUSSION

3.1 Morphology of TiO$_2$ NT arrays. TiO$_2$ NTs growth during Ti anodization in organic solvents containing water and fluoride ions proceeds through two steps, *i.e.*, *i*) the electric-field-assisted formation of a dense TiO$_2$ layer at the metal surface, according to the reaction: Ti + 2 H$_2$O → TiO$_2$ + 2 H$^+$ + 2 e$^-$; *ii*) the both field-assisted and chemical dissolution at the oxide/electrolyte interface of the so produced oxide layer, due to the formation of the soluble Ti[F$_6$]$^{2-}$ complex.[7] Whereas the field-assisted processes takes place at the NTs bottom, chemical dissolution can occur along the whole NT surface. At the same time, H$_2$ evolution occurs at the Pt cathode. Because of the competition between oxide formation and its dissolution, NT formation can be obtained only in the presence of an optimal fluoride concentration (usually 0.05 M < F$^-$ < 0.5 M). Different morphology aspects of typical TiO$_2$ NTs can be appreciated in Figure 1, showing several SEM images obtained from a NT film etched by gently scratching it with a cutter tip (Figure 1A). By this way small fragments of the film were detached, which randomly rotated over the NTs film surface, as shown in Figure 1C and 1F. In particular, Figure 1C displays a SEM micrograph of a film fragment rotated by 180° showing the typical closed and hemispherically shaped bottom of the NTs, together with a limited view of the NTs cross section (lower part of Figure 1C), revealing the characteristic inner V-shape of TiO$_2$ NTs (*i.e.* their wall thickness increases towards the bottom).[26,27] Moreover, the thickness of the NTs bottom (the barrier layer) increases with increasing anodization time and applied potential.[28]
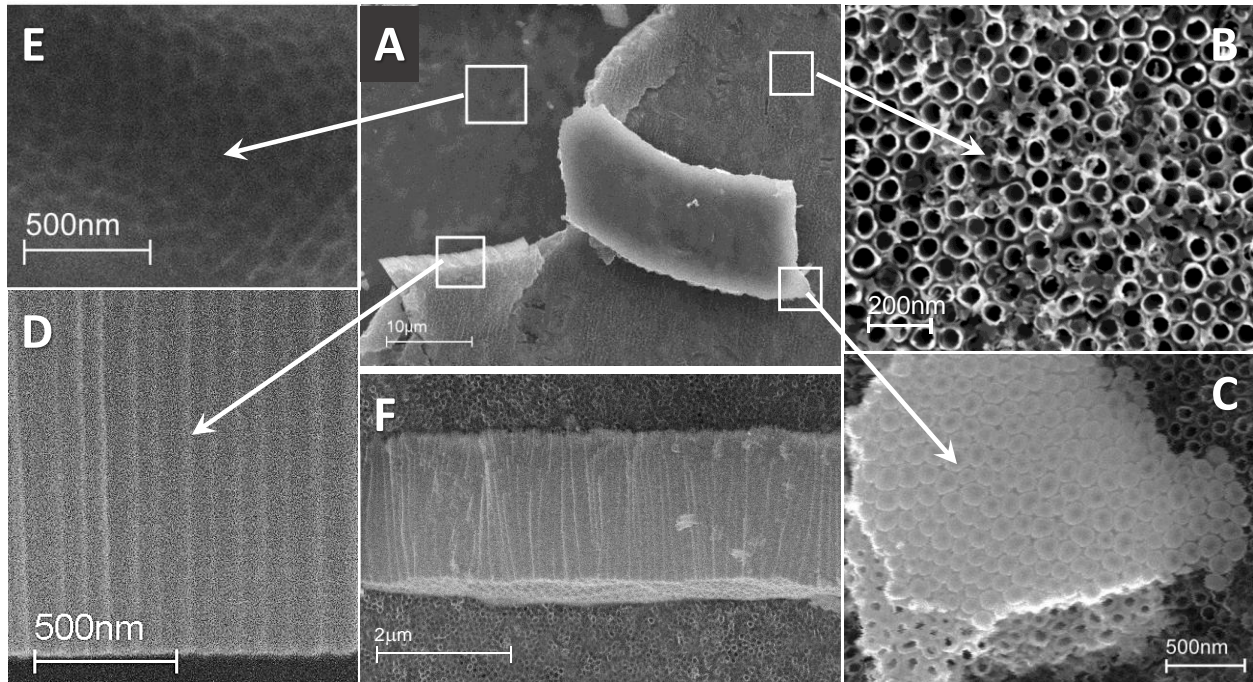
Figure 1. (A) SEM image along a mechanical scratch over a TiO$_2$ NT film with the magnification of (B) the top, (C) the bottom and (D) the side views of the NTs, together with (F) a fragment of NT film showing the film thickness, and of (E) the metal Ti surface underneath the NT film.

The detachment of the NTs film leaves a pattern of little grooves on the metal Ti surface (Figure 1E) specular to the NTs bottom. In the two steps anodization process adopted in the present work the formation of this pattern is exploited to obtain more homogeneous and better-aligned NTs array. The top view of the NTs film (Figure 1B) shows a rather homogeneous surface characterized by the hexagonally shaped, closely packed NTs open mouths. The fragments rotated by 90° (Figure 1 F and 1D) exhibit the side morphology of the NT array consisting of well self-assembled and vertically aligned individual NTs. These micrographs were used to measure the thickness of the TiO$_2$ NT films (*i.e.* the NTs length).

Figure 2 shows that, as expected, the NTs length linearly increases with increasing the anodization time under the here adopted anodization conditions, up to *ca* 120 min.
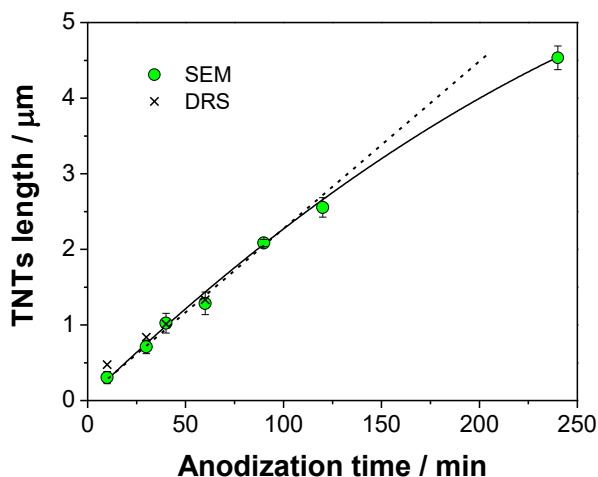

Figure 2. Length of TiO_2 NTs determined from SEM micrographs and by UV-vis-NIR DR spectroscopy as a function of the anodization time under 50 V constant applied potential.

After 2 h the NTs growing rate decreases with increasing anodization time because chemical dissolution becomes predominant leading to an extended etching of the NTs top. Moreover, a prolonged exposure to the fluoride containing electrolyte leads to the appearance of undesired irregularly shaped oxide aggregates laying over the top of the tubes, commonly called "nanograss".[6,7] The NTs growing rate, which can be obtained from the slope of the linear part of the curve shown in Figure 2, is also affected, among other parameters, by the potential applied during the anodization process. Furthermore, by increasing the anodization potential both the inner NTs diameter (Figures 3 and 4) and the NTs growing rate (Figure 3) linearly increase. Moreover, Figure 4 shows that the wall thickness (*ca.* 10±1 nm) at the top of the TiO_2 NTs is not substantially affected by the applied potential, at least under the here investigated experimental conditions and applied potential range.
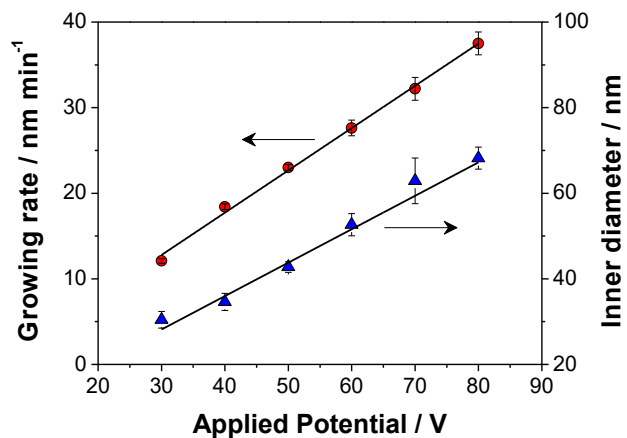
Figure 3. Effect on the NTs growing rate and inner diameter of the potential applied during Ti anodization.
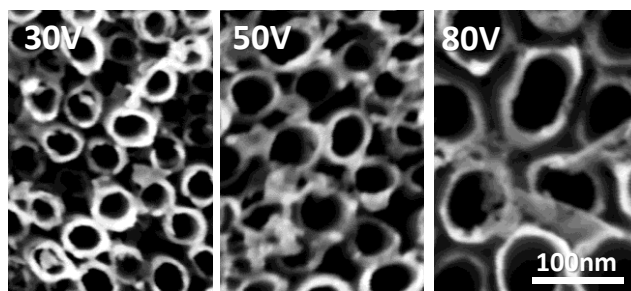

Figure 4. Top view FESEM micrographs of TiO_2 NT arrays synthesized by Ti anodization in a H_2O and HF containing ethylene glycol electrolyte solution at 30 V, 50 V and 80 V for 1.21 h, 0.72 h and 0.45 h, respectively.

3.2 XRD investigation. The as prepared self-assembled, vertically oriented TiO_2 NT arrays are notoriously amorphous, their XRD patters being dominated by the reflections of the underneath metal Ti foil. A post calcination treatment is therefore necessary to confer them the crystallinity required for photocatalytic applications. The main peaks of crystalline TiO_2 appear after calcination at 450 °C (Figure 5).
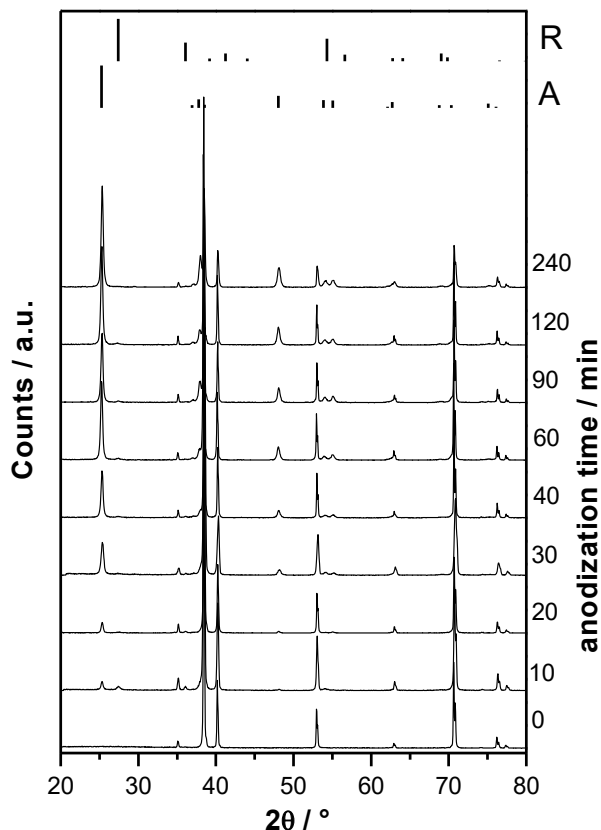
11

Figure 5. XRD patterns of pristine Ti foil and of TiO$_2$ NTs films grown by anodization at 50 V for different times, followed by calcination at 450 °C. The peaks position and relative intensity of anatase (A) and rutile (R) are reported on the top of the figure for comparison.

Their intensity increases with increasing the anodization time whereas those of the Ti foil decrease in parallel, in agreement with the increasing thickness of the NTs films. All NT arrays prepared with anodization times above 20 min show only the reflections characteristic of the anatase crystal structure. By contrast, the sample prepared by 10 min – long anodization (*i.e.* the thinner one of the series) exhibits the reflections of rutile as well, due to the fact that rutile grows at the interface between metallic Ti and the NT bottom, where the metal undergoes thermal oxidation during the calcination process.[6,8] The series of NT arrays obtained at different applied potentials (30 to 80 V) by adjusting the anodization time so as to keep the NTs length fixed at 1

μm shows similar XRD patterns (Figure S1 in the supporting information), typical of pure anatase.

3.3 Diffuse reflectance UV-vis-NIR spectroscopy. The UV-vis-NIR DR spectra recorded in the 220 nm $< \lambda <$ 2600 nm range are shown in Figure 6, with the abscissa axis in energy. In the vis-NIR region the NTs thin films synthesized with anodization times up to 60 min display the typical fringes originated by the interference of waves reflecting off the top surface with those propagating through the film and reflecting from the bottom surface. The frequency of the fringes increases and their amplitude decreases with increasing film thickness. The film thickness d (*i.e.* the NTs length) can be calculated from the interference fringes as follows. The reflectance is approximately π periodic in kd (where k is the component of the wavevector normal to the film), *i.e.* if λ_1 and λ_2 are two consecutive peaks or valleys wavelengths, the following equation holds:

$$2\left(\frac{1}{\lambda_1} - \frac{1}{\lambda_2}\right) n \cdot cos(\phi')d = 1$$

where n is the refractive index of the film (*ca.* 2.5 for anatase in the range 450-600 nm) and ϕ' the refraction angle. Using the Snell's law to replace ϕ' with the incidence angle ϕ one obtains:

$$d = \frac{1}{2\sqrt{n^2 - n_a^2 sin^2\phi}} \cdot \frac{\lambda_1 \cdot \lambda_2}{\lambda_1 - \lambda_2}$$

where n_a is the refractive index of the incidence medium ($n_a = 1$ for air). This result holds irrespectively of the properties of the supporting substrate (*e.g.* Ti), provided its reflectivity is approximately constant in the spectral region of interest. The d values calculated by this equation are in very good agreement with the NTs length determined by SEM analysis (see Figure 2).
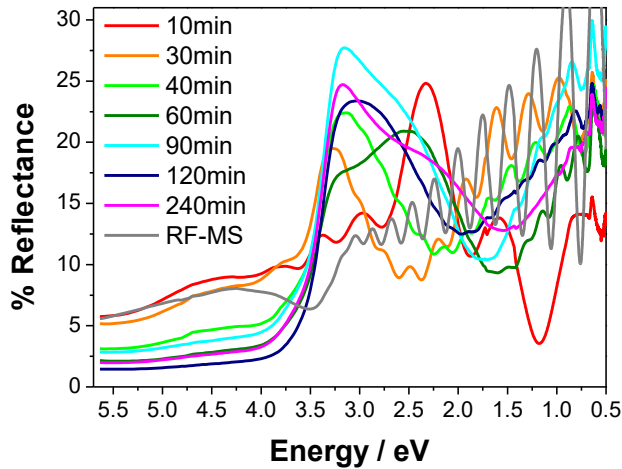
Figure 6. UV-vis-NIR DRS spectra of TiO$_2$ NTs films grown by anodization at 50 V for different times, followed by calcination at 450°C. The spectrum of an anatase TiO$_2$ dense film prepared by RF-Magnetron Sputtering (gray curve) is also shown for comparison.

Also reported in Figure 6 is the DR spectrum of a *ca.* 1 μm thick film consisting of randomly packed TiO$_2$ anatase nanoparticles produced by Radio Frequency Magnetron Sputtering (gray curve in Figure 6). The NTs films display increased reflectance just before the semiconductor absorption threshold that might be due to the overlapping with the photonic band gap. Such increase of reflectance does not occur in the dense film made by Magnetron Sputtering, because it does not have photonic crystal properties.

The absorption edge of the NTs films are all located around 3.2 eV, which is typical of bulk anatase, independently of the anodization time or applied voltage (see also Figure S2 in the supporting information). Overlapping of the absorption edge with the interference fringes is particularly evident in the case of the thinner film (10 min anodization time). Moreover, the absorption step increases and the reflectance in the UV region decreases with increasing the anodization time (*i.e.* the film thickness) up to 2 μm – thick films (obtained by 90 min

anodization time). This suggests that *ca.* 2 μm is the maximum penetration depth of the incident light in TiO$_2$ NTs.

3.4 Photonic bandgap theoretical calculation. The typical photonic band structure calculated for a 35 Å NT inner radius is shown in Figure 7.
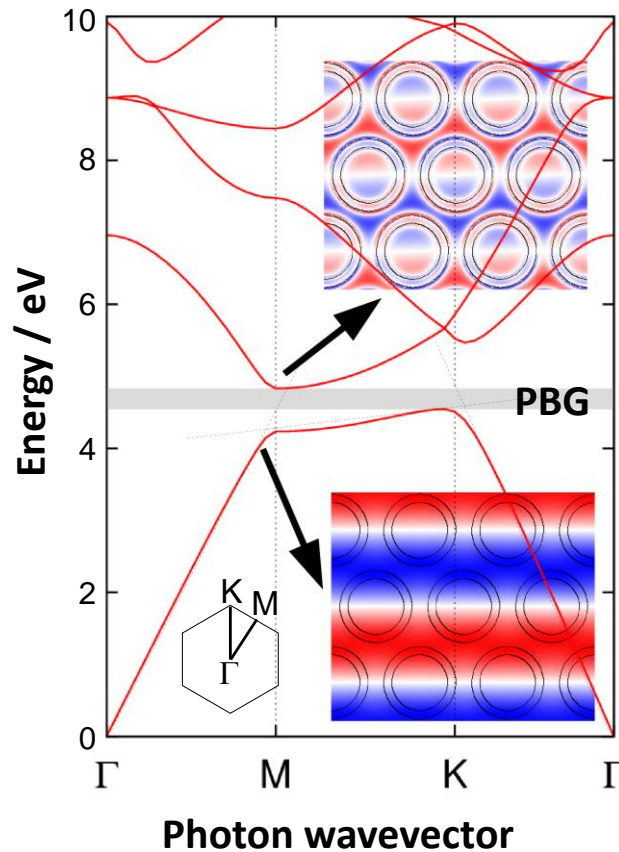

Figure 7. Photonic bands structure of TiO$_2$ NT arrays with 35 nm inner radius, 10 nm wall thickness and 20 nm gap between the tubes. The photonic bandgap is highlighted by a gray stripe. The two insets show the electromagnetic field localization at the air and dielectric bands.

Only the first few modes are shown as a function of the photon momentum. The resulting dispersion for the lowest mode (the light mode) is linear for small momenta and it shows a forbidden bandgap at about 4.5 eV. This interval of forbidden photon energies is located above the TiO$_2$ anatase absorption threshold (typically 3.2 eV). The obtained value is very likely

15

overestimated, because a frequency-independent dielectric constant was used for anatase. In fact, the solver implemented in the MIT Photonic-Bands code (MPB) [24] does not allow either frequency-dependence or an imaginary part of the dielectric constant. This limitation of the computational method prevents a direct prediction of the PBG position of our TiO_2 NTs film. Despite this limitation, very important qualitative information can be obtained on the dependence of the photonic bandgap position on geometrical parameters (Figure 8). Indeed, our simulations show that the photonic gap shifts to lower energy (higher wavelength) as the tube radius increases (Figure 8A). For a tube inner radius of 50 Å the photonic gap falls below the anatase absorption threshold. Interestingly, there is a maximum value for the tube radius, beyond which the photonic gap vanishes.
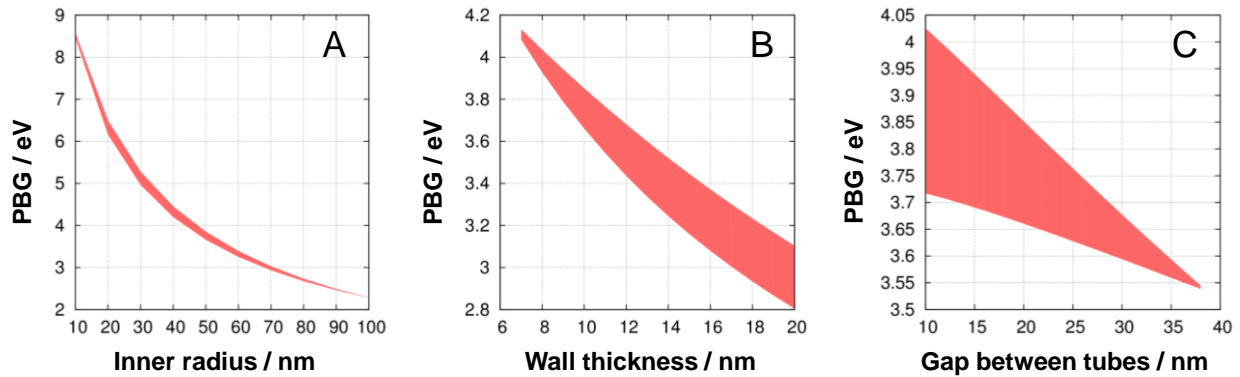

Figure 8. Effect on the PBG position of TiO_2 NTs (A) inner radius, (B) tube thickness and (C) gap between tubes.

The band gap also shifts to lower energy and widens as the tube thickness increases (Figure 8B). In this case, there is a minimum thickness, below which the photonic gap closes. The dependence of the photonic gap is less affected by the spacing of the tubes (Figure 8C), but if the tubes are made further apart, our calculation predicts a vanishing bandgap. Therefore, there is a very good agreement on a quantitative level between present experimental results and

calculations, and a photonic bandgap is expected for hollow tubes in a narrow range of geometric parameters (radius, thickness, and distance), around those reported in this work. Moreover, the most important result arising from these calculations is the possibility of tuning and engineering the PBG position so that it falls in the most convenient photonic energy position, by simply adjusting the proper TiO_2 NT synthesis parameters.

The insets in Figure 7 show the localization of the electromagnetic field at the blue (air band) and red (dielectric band) edges of the PBG. As already mentioned above, at the high energy band the light traveling perpendicular to the NT arrays is predominantly localized in the empty spaces, *i.e.* air or water (low dielectric medium). By contrast, at the low energy band the light is predominantly focused on the TiO_2 NTs walls (high dielectric medium) leading to an increased photonic density on the semiconductor material. This is a peculiar characteristic of photonic crystals. Indeed, in dense and randomly packed films of TiO_2 nanoparticles light propagates as a flat wave.

3.5 IPCE measurements. The photocurrent curves measured as a function of the incident wavelength exhibit a Gaussian-like shape (Figure 9A and B). Indeed, the photocurrent increases with increasing wavelength because of the increasing incident light power (gray curve in Figure 9B) followed by a photocurrent decrease above the semiconductor absorption edge. All films prepared by increasing the anodization time show a photocurrent maximum located at 344 nm. As shown in Figure 9C and in Figure 10, at the beginning the maximum IPCE linearly increases with increasing the anodization time (*i.e.* with increasing the NTs length) reaching a maximum of 25% for the NTs array anodized for 40 min (1 μm length). Above this time the maximum IPCE slightly decreases and reaches a plateau above 90 min (2 μm length).
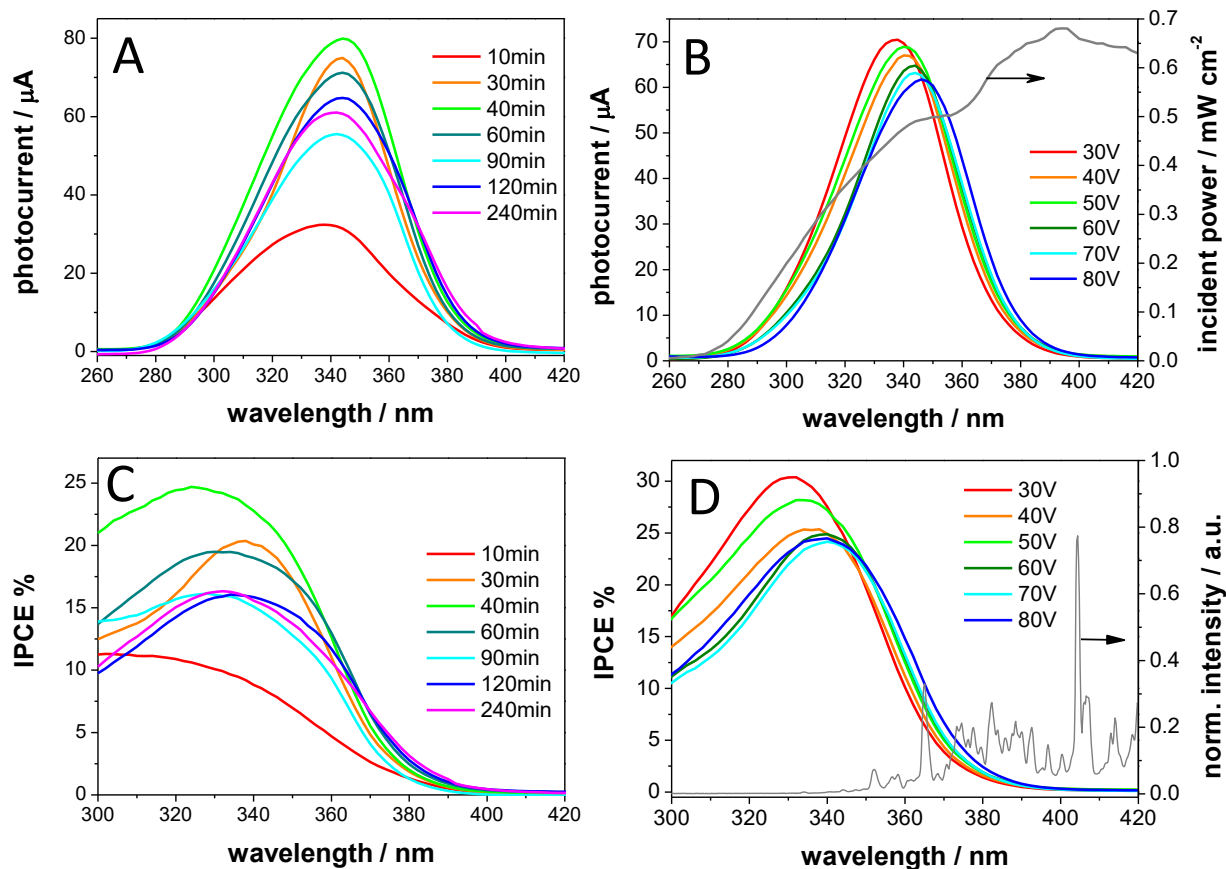
Figure 9. Effect of (A, C) anodization time and (B, D) applied potential on (A, B) photocurrent and (C, D) IPCE as a function of the incident wavelength. The gray curves in B and D are the incident power of the Xe lamp used for the IPCE measurements and the spectrum of Hg vapor lamp used for separate H_2 and O_2 evolution photocatalytic tests, respectively.

The initial maximum IPCE growth can be ascribed to the increasing NTs length leading to a surface area and incident photon absorption efficiency enhancement up to the maximum light penetration depth (*i.e.*, 2 μm as suggested by the DR analysis in Figure 6). Above this limit the maximum IPCE decreases because the beneficial effect of further surface area growth is compensated by the longer percolation path for photopromoted electron transfer, with a consequent higher probability of electron-hole recombination. Moreover, longer NTs can introduce mass transfer limitations due to penetration and diffusion of the electrolyte and of the

produced O_2 along the NT pores.[29] These results demonstrate that the optimal NTs length under the investigated preparation conditions is 1 μm.
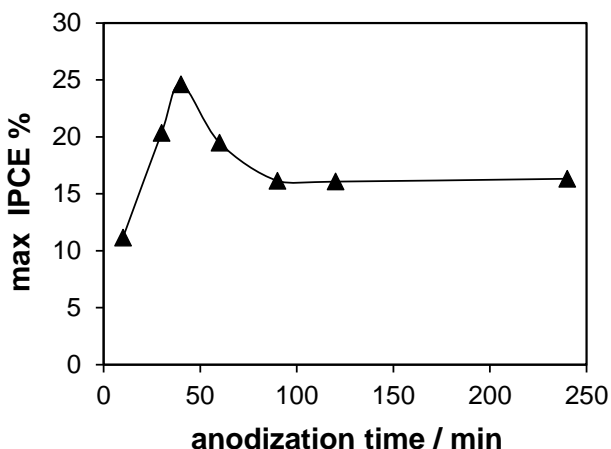

Figure 10. Effect of the anodization time (*i.e.*, TiO_2 NTs length) on the maximum IPCE.

Based on this result, the second series of films was prepared at different applied potential by adjusting the anodization time in order to keep the NTs length fixed at *ca.* 1 μm (Table 1). This allowed a systematic investigation on the effect of the sole tube diameter on the photocatalytic performance of the NT arrays. The so obtained photocurrent measurements and IPCE results are presented in Figure 9B and D, respectively. All photocurrent curves are characterized by a similar magnitude in agreement with the similar NTs length (Figure 9B). The maximum IPCE linearly decreases with increasing the NT pores diameter (Figure 11), very likely because of the decreased surface area for geometrical reasons.

However, the most relevant result is the red shift of the photocurrent curves (Figure 9B) with increasing NT pores diameter that provokes a likewise red shift of the photoactivity threshold (Figure 9D), as underlined by the linear shift of the first derivative minimum of the IPCE curves (Figure 11).
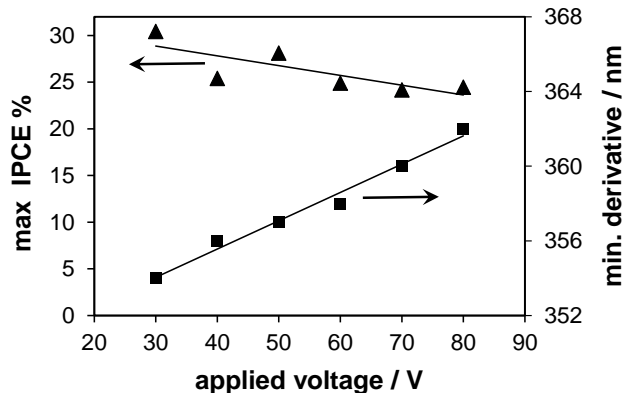
Figure 11. Effect of applied potential (*i.e.*, TiO$_2$ NTs pore diameter) on the maximum IPCE and on the minimum of the first derivative of the IPCE curves.

This result, achieved by simply changing the pore diameter without any chemical doping or electronic structure variation, has an important impact in the frame of solar light harvesting and conversion. In particular, the red shift can be explained by considering the parallel red shift of the PBG position as shown in Figure 8A. Indeed, in a perfect photonic crystal the presence of a PBG can be expected to decrease the absorption efficiency because of the total reflection properties. However, several defects are present in the periodical structural arrangement of our NT arrays produced by Ti anodization, which can act as gates for light penetration inside the film, where it is then confined. Thus, the red shift of the maximum photocurrent can be ascribed to the increased absorption probability of these trapped photons. Moreover, the red shift of the IPCE threshold can be attributed to the parallel shift of the dielectric band which improves the photons absorption efficiency thanks to the generation of the slow photons and the localization of the electromagnetic field on the TiO$_2$ NT walls. By contrast, at the high energy band (at lower wavelengths) the electromagnetic field is predominantly localized on water causing the parallel shift (photocurrent decrease) at lower wavelengths with increasing the TiO$_2$ NTs pore diameter.

3.6 Separate H$_2$ and O$_2$ production. In the previous section we showed that an increase of the NTs inner diameter leads to a red shift of the IPCE curves (Figure 9D) thanks to the parallel shift of the PBG. These curves together with the emission spectrum of the employed light source (Figure 9D) can be used to calculate the *expected quantum efficiency in H$_2$ production* (ϕ_{exp}) under polychromatic irradiation (*i.e.* the "expected portion of converted spectrum"), obtained as the product of the IPCE curve times the emission spectrum of the lamp (Figure S3). Thus, ϕ_{exp} can be calculated as the ratio of the integral of these curves over the integral of the whole incident spectrum in the $300 < \lambda < 400$ nm range. The obtained results are presented in Figure 12 and in Table1.
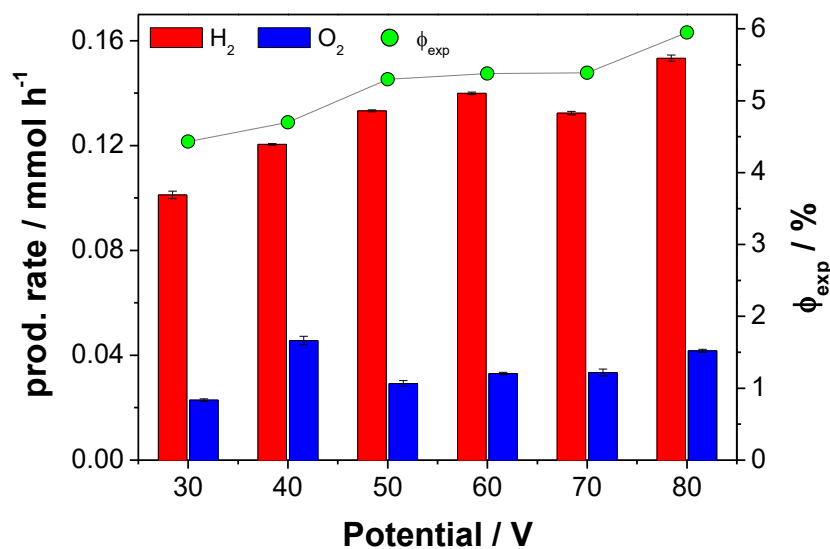

Figure 12. Effect of anodization applied potential on the rates of photocatalytic H$_2$ and O$_2$ production and on the expected quantum efficiency ϕ_{exp}.

The H$_2$ production rates calculated by the produced gas collected in the graduated burettes placed above the two electrodes are in agreement with those calculated by the photocurrent profiles (Figure S4), as shown in Table1. The H$_2$ production rate significantly increases with increasing the NTs inner diameter. In particular, a remarkable 50% increment of the H$_2$

production rate was attained by simply increasing the inner diameter from 35 nm (0.101 mmol H_2 / h) to 70 nm (0.153 mmol H_2 / h).

Table 1. Effect of applied potential during the anodization synthesis of the TiO_2 NTs array films on the hydrogen (r_{H_2}) and oxygen (r_{O_2}) production rates and on the expected quantum efficiency (ϕ_{exp})

Applied potential / V	Anodization time / min	r_{H_2} / mmol h^{-1}		ϕ_{exp} / %	r_{O_2} / mmol h^{-1}
		from gas	from photocurrent		
30	72	0.101	0.110	4.43	0.023
40	54	0.120	0.122	4.70	0.039
50	43	0.133	0.142	5.30	0.029
60	36	0.140	0.147	5.38	0.033
70	31	0.132	0.144	5.39	0.033
80	27	0.153	0.154	5.95	0.042

Because the H_2 production rate follows the same trend as ϕ_{exp}, the improved photoactivity can be ascribed to the red shift of the IPCE curve that allows harvesting and converting a larger portion of the incident lamp spectrum thanks to the exploitation of the photonic crystal properties of the NTs array film. A similar effect of the anodization voltage on the H_2 production rate was recently reported by Sun and Yan,[10] who synthesized a series of NTs films with the same anodization time at each applied potential and attributed the observed trend to the increased surface area consequent to the longer tubes. By contrast, here we are able to discern the effect of the sole inner diameter variation by comparing films with the same NTs length. This allows us to

discuss our results in terms of photonic crystal properties, as supported by the IPCE measurements.

4. CONCLUSIONS

This work demonstrates that the photonic crystal properties typical of ordered periodic structures can be profitably exploited to increase the efficiency of solar light harvesting and conversion and the photocatalytic performance of TiO_2 NT arrays-based photoanodes. This can be attained taking advantage of three characteristics of the photonic band structure: *i*) the PBG can be used to confine the incident light of proper wavelength within the TiO_2 NTs film; *ii*) the dielectric band can be used to concentrate the incident photons of corresponding wavelength on the TiO_2 NTs walls; and *iii*) the absorption efficiency of these photons is further boosted by their reduced group velocity (slow photons) due to the flattening of the photonic band in certain propagation directions. Theoretical calculations demonstrate that the position and width of the PBG are both affected by TiO_2 NTs inner diameter, wall thickness and distance between the pores. Thus, the PBG can be easily tuned by adjusting the TiO_2 NTs synthesis parameters in order to fit with the semiconductor absorption band aiming at red shifting the photoactivity threshold. By this way a 50% higher H_2 production rate under polychromatic irradiation was attained by simply increasing the inner TiO_2 NT diameter. This important result can in principle be transferred to any other semiconductor material and can be exploited in the field of solar fuels production to harvest and convert a larger portion of the solar spectrum.

ASSOCIATED CONTENT

Supporting Information. The following files are available free of charge: XRD and UV-vis-NIR DRS of the series of TiO_2 NTs films prepared at different applied potential, expected

portion of converted incident lamp spectrum and photocurrents measured during separate H_2 and O_2 photocatalytic tests are shown in the supporting information (PDF).

AUTHOR INFORMATION

Corresponding Author

* E-mail: gianluca.chiarello@unimi.it

Notes

The authors declare no competing financial interests.

ACKNOWLEDGMENT

REFERENCES

(1)   Lu, Y.; Yu, H.; Chen, S.; Quan, X.; Zhao, H. *Environ. Sci. Technol.* **2012**, *46*, 1724–1730.

(2)   Li, J.; Wu, N. *Catal. Sci. Technol.* **2015**, *5*, 1360–1384.

(3)   Lianos, P. *J. Hazard. Mater.* **2011**, *185*, 575–590.

(4)   Walter, M. G.; Warren, E. L.; McKone, J. R.; Boettcher, S. W.; Mi, Q.; Santori, E. a.; Lewis, N. S. *Chem. Rev.* **2010**, *110*, 6446–6473.

(5)   Selli, E.; Chiarello, G. L.; Quartarone, E.; Mustarelli, P.; Rossetti, I.; Forni, L. *Chem. Commun.* **2007**, 5022–5024.

(6)   Altomare, M.; Pozzi, M.; Allieta, M.; Bettini, L. G.; Selli, E. *Appl. Catal. B Environ.* **2013**, *136-137*, 81–88.

(7)   Roy, P.; Berger, S.; Schmuki, P. *Angew. Chemie - Int. Ed.* **2011**, *50*, 2904–2939.

(8)   Mor, G. K.; Varghese, O. K.; Paulose, M.; Shankar, K.; Grimes, C. a. *Sol. Energy Mater. Sol. Cells* **2006**, *90*, 2011–2075.

(9)   Xue, Y.; Sun, Y.; Wang, G.; Yan, K.; Zhao, J. *Electrochim. Acta* **2015**, *155*, 312–320.

(10)   Sun, Y.; Yan, K. P. *Int. J. Hydrogen Energy* **2014**, *39*, 11368–11375.

(11)   Regonini, D.; Clemens, F. J. *Mater. Lett.* **2015**, *142*, 97–101.

(12)   Lynch, R. P.; Ghicov, A.; Schmuki, P. *J. Electrochem. Soc.* **2010**, *157*, G76–G84.

(13)   Joannopoulos, J. D.; Villeneuve, P. R.; Fan, S. *Nature* **1997**, *386*, 143–149.

(14)   Chen, J. I. L.; von Freymann, G.; Choi, S. Y.; Kitaev, V.; Ozin, G. A. *J. Mater. Chem.* **2008**, *18*, 369–373.

(15)   Chen, J. I. L.; Von Freymann, G.; Choi, S. Y.; Kitaev, V.; Ozin, G. A. *Adv. Mater.* **2006**, *18*, 1915–1919.

(16)   Chen, H.; Chen, S.; Quan, X.; Zhang, Y. *Environ. Sci. Technol.* **2010**, *44*, 451–455.

(17)   Wu, M.; Liu, J.; Jin, J.; Wang, C.; Huang, S.; Deng, Z.; Li, Y.; Su, B. L. *Appl. Catal. B Environ.* **2014**, *150-151*, 411–420.

(18)   Liu, J.; Liu, G.; Li, M.; Shen, W.; Liu, Z.; Wang, J.; Zhao, J.; Jiang, L.; Song, Y. *Energy Environ. Sci.* **2010**, *3*, 1503.

(19)   Chen, J. I. L.; Ozin, G. a. *J. Mater. Chem.* **2009**, *19*, 2675.

(20)   Sordello, F.; Minero, C. *Appl. Catal. B Environ.* **2015**, *163*, 452–458.

(21)   Sordello, F.; Duca, C.; Maurino, V.; Minero, C. *Chem. Commun.* **2011**, *47*, 6147–6149.

(22)   Zhang, Z.; Zhang, L.; Hedhili, M. N.; Zhang, H.; Wang, P. *Nano Lett.* **2013**, *13*, 14–20.

(23)   Al-Haddad, A.; Wang, Z.; Xu, R.; Qi, H.; Vellacheri, R.; Kaiser, U.; Lei, Y. *J. Phys. Chem. C* **2015**, *119*, 16331–16337.

(24)   Johnson, S.; Joannopoulos, J. *Opt. Express* **2001**, *8*, 173–190.

(25)   Jellison, G. E.; Boatner, L. a.; Budai, J. D.; Jeong, B. S.; Norton, D. P. *J. Appl. Phys.* **2003**, *93*, 9537–9541.

(26)   Albu, S. P.; Ghicov, A.; Aldabergenova, S.; Drechsel, P.; LeClere, D.; Thompson, G. E.; Macak, J. M.; Schmuki, P. *Adv. Mater.* **2008**, *20*, 4135–4139.

(27)   Macak, J. M.; Albu, S. P.; Schmuki, P. *Phys. Status Solidi - Rapid Res. Letetrs* **2007**, *1*, 181–183.

(28)   Apolinário, A.; Quitério, P.; Sousa, C. T.; Ventura, J.; Sousa, J. B.; Andrade, L.; Mendes, a. M.; Araújo, J. P. *J. Phys. Chem. Lett.* **2015**, *6*, 845–851.

(29)   Kim, D.; Macak, J. M.; Schimidt-Stein, F.; Schmuki, P. *Nanotechnology* **2008**, *19*, 305710.

TOC GRAPHICS